Newton

Article

Modeling of current-voltage characteristics of high-efficiency kesterite solar cells

Graphical abstract

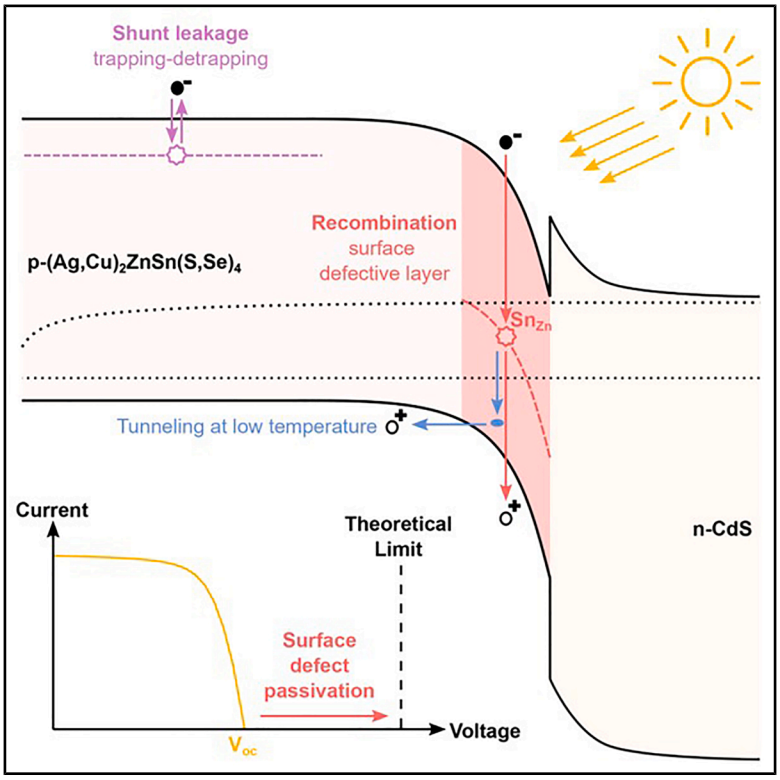

Highlights

- State-of-the-art kesterite solar cells closely follow single diode formalism
- Dark and light reconciliation attests close-to-ideal current-voltage behavior
- Defective kesterite layer hypothesized as main open-circuit voltage-limiting factor
- Carrier trapping via shallow states greatly contributes to shunt currents

Authors

Romain Scaffidi, Alex Jimenez-Arguijo, Yuancai Gong, ..., Edgardo Saucedo, Denis Flandre, Bart Vermang

Correspondence

romain.scaffidi@imec.be

In brief

Kesterite-based solar cells do not typically show close agreement with the idealistic single diode model. Scaffidi et al. demonstrate that the optoelectronic quality enhancements in recent solution processing baselines for kesterite thin films lead to a closer-to-ideal behavior, remarkably reconciling dark and light responses. Through robust device modeling, the dominant source of losses in the device is identified as a defect-rich layer restraining its voltage output, while light is also shed on the mechanism responsible for leakage currents.

Scaffidi et al., 2025, Newton *1*, 100198
October 6, 2025
https://doi.org/10.1016/j.newton.2025.100198

CellPress

Newton

CellPress
OPEN ACCESS

Article

Modeling of current-voltage characteristics of high-efficiency kesterite solar cells

Romain Scaffidi,[1,2,3,4,8,*] Alex Jimenez-Arguijo,[5,6] Yuancai Gong,[5,6] Guy Brammertz,[1,2,3] Arindam Basak,[7] Zacharie Jehl Li-Kao,[5,6] Edgardo Saucedo,[5,6] Denis Flandre,[4] and Bart Vermang[1,2,3]

[1]imo-imomec, Hasselt University, Martelarenlaan 42, Hasselt 3500, Belgium
[2]imo-imomec, imec, Thor Park 8320, Genk 3600, Belgium
[3]imo-imomec, EnergyVille, Thor Park 8320, Genk 3600, Belgium
[4]ICTEAM, UCLouvain, Place du Levant 3, Louvain-la-Neuve 1348, Belgium
[5]Electronic Engineering Department, Universitat Politècnica de Catalunya, Avenida de Eduard Maristany 10-14, Barcelona 08019, Spain
[6]Barcelona Center for Multiscale Science & Engineering, Universitat Politècnica de Catalunya, Avenida de Eduard Maristany 10-14, Barcelona 08019, Spain
[7]Thin Film Photovoltaic Lab, School of Electronics Engineering, Kalinga Institute of Industrial Technology (KIIT), Bhubaneswar, Odisha 751024, India
[8]Lead contact
*Correspondence: romain.scaffidi@imec.be
https://doi.org/10.1016/j.newton.2025.100198

ACCESSIBLE OVERVIEW Kesterite thin-film solar cells recently regained interest from the scientific community due to performance breakthroughs allowed by fine regulation of both their composition and their electronic defect landscape, facilitated by a transition to molecular ink chemical processes. In order to update the current understanding of these devices, this work dives deep into their optoelectrical response. A comprehensive and robust analysis of temperature- and light-intensity-dependent current-voltage measurements is developed. The lower crystalline disorder and potential fluctuations in next-generation kesterite absorbers enable excellent agreement with the well-established single diode model in a broad temperature range, reconciling dark and light behaviors—an uncommon achievement in inorganic thin-film photovoltaics. Based on this theoretical framework in combination with simulations, this study establishes links between the device behavior and important material properties, as well as dominant recombination mechanisms, while also providing practical conditions for photovoltaic devices to be well behaved. This work advances the in-depth understanding of kesterite solar cell behavior in relevant conditions by hypothesizing the critical role of a defect-rich layer at the top absorber surface as the primary performance-limiting factor. Quantifying its impact on the open-circuit voltage deficit demonstrates its large dominance compared to other loss mechanisms, suggesting important guidelines for further efficiency enhancement. Reverse currents are also thoroughly inspected, allowing one to pinpoint shallow defect states as the potential origin of shunt currents in the studied device and possibly in other thin-film chalcogenide solar cells as well. The applicability of this analysis is demonstrated over various samples, strengthening the conclusions and calling for further extension to other device types.

SUMMARY

The recent developments in baselines for kesterite photovoltaic absorbers raise the need for an update of the models used to understand their current-voltage behavior. In particular, the large efforts devoted to mitigating band tailing and control defect formation via molecular ink routes provide kesterite compounds with a more ideal optoelectronic landscape. This study demonstrates, via a robust analysis procedure of temperature- and light-intensity-dependent current-voltage measurements, that such material enhancements translate into a closer-to-ideal response of kesterite devices within the single diode formalism. Excellent model agreement is reached in the dark for a broad temperature range, allowing one to draw solid hypotheses about the main recombination channels. Remarkably, these observations can be reconciled with the sample response under light, implying strategies for future performance gains. Eventually, dark reverse currents reveal that shunt leakages, especially critical for indoor applications, may actually originate in shallow defect states rather than classical ohmic conduction.

INTRODUCTION

Kesterite-based solar cells have recently seen significant improvements in their efficiency, up to 15%,[1] and could potentially become an economically viable, non-toxic, and sustainable alternative to commercial thin-film photovoltaic (PV) devices relying on Cu(In,Ga)Se_2 (CIGS) and CdTe. This was mostly achieved through defect regulation by cationic alloying[2,3] and monitored growth environment[4] and control of the phase formation at both the precursor[5] and the annealing[6] levels, as well as improvements in the kesterite/CdS interface (IF) quality.[7] All these strategies are targeting the main performance-limiting factor in kesterites, i.e., their high open-circuit voltage (V_{oc}) deficit.[8] This metric is closely linked to non-radiative recombination, especially in highly defective compounds such as kesterites.[9–11] To reach further efficiency enhancements, a deeper understanding of their optoelectrical behavior and the dominant recombination path is required. The analysis of the current-voltage response of a solar cell within the single diode model formalism proves particularly useful in that regard, as it establishes a direct relationship between the V_{oc} and the intrinsic electronic properties of the pn diode. Therefore, understanding which underlying mechanisms are governing the model parameters is key to determine strategies for counteracting the V_{oc} deficit.

The need for a refined device state-of-the-art modeling is even greater given the recent developments within the kesterite baselines. On the one hand, large reductions in radiative V_{oc} losses were obtained through mitigated band tailing and potential fluctuations,[2–4,12,13] which were a main culprit of divergence with the standard single diode model in previous nanoparticle-based samples, as previously reported.[14] On the other hand, most of the current best-performing devices are based on kesterite absorbers deposited via molecular ink chemical routes,[2,3,6] which, at the current laboratory-scale development, provide good control and reproducibility.[15] The kesterite solar cells resulting from such solution-based processes exhibit reduced shunt leakage, making them well suited to indoor-environment applications.[16] This emphasizes the interest in investigating the underlying mechanisms by exploring the device response in the reverse bias regime.

To do so, this work proposes a unified and comprehensive analysis of temperature-dependent current-voltage measurements realized in both dark and light and in both forward and reverse biases on high-quality solution-processed Ag-alloyed kesterite devices. The presented methodology leads to important conclusions about material quality, device behavior, and performance improvement pathways, based solely on the measurement of a single physical quantity, i.e., the current density (J), in the function of the voltage (V), temperature (T), and light intensity (I), denoted as JVTI in the following. The first part of this study concerns the analysis of dark JVT experiments, highlighting the existence of a broad range of temperature, in which close agreement with the unaltered single diode model is reached. Based on this robust modeling, the two cases of bulk- and IF-limited recombination are discussed, relying on SCAPS-1D[17] simulations to complement previously established theoretical models. This leads to the hypothesis of a thin defective kesterite layer close to the absorber/buffer IF dominating recombination in the studied devices at room temperature, while the importance of determining the buffer carrier concentration is stressed. At lower temperatures, the enhancement of recombination by tunneling enables one to explain the divergence from the single diode model. The second part focuses on JVTI measurements and demonstrates a remarkably weak dark-light discrepancy in the sample response, indicating not only a closer-to-ideal optoelectrical behavior but also a common dominant recombination channel in either dark or light conditions. This allows one to quantify the potential V_{oc} gains and confirm the pivotal role of the ideality factor n and saturation current prefactor J_{00} regarding non-radiative losses in kesterite solar cells. Finally, the last part describes a preliminary exploration of the dark JVT data in reverse bias, shedding light on carrier trapping-detrapping via shallow defects as a potential physical origin of shunt currents.

RESULTS

The goal of this study is to gauge if the single diode model can predict the behavior of new-generation thin-film solar cells with $(Ag,Cu)_2ZnSn(S,Se)_4$ (ACZTSSe) kesterite absorbers, despite the usual non-ideal character of such devices. To achieve this, an analysis methodology is herein built based on one central sample called A1, while its validity for other samples, A2, A3, and B, is demonstrated in the supplemental information, with the details about all samples provided in the methods. The central mathematical expression for the single diode model used in this work is

$$J(V,T) = J_{ph}(V,T) - J_0(T)\left[\exp\left[\frac{q(V+R_s(T)J)}{n(T)k_BT}\right] - 1\right] - \frac{V+R_s(T)J}{R_{sh}(T)}, \quad \text{(Equation 1)}$$

with q being the elementary charge (in C) and k_BT the thermal energy (in eV). The saturation current density J_0 (in A/cm^2) and the unitless ideality factor n are the two diode parameters characterizing the ACZTSSe/CdS pn diode heterojunction (HJ). The series resistance R_s and shunt resistance R_{sh} (in $\Omega.cm^2$) are parasitic elements. The second key equation in this study provides the temperature dependence of J_0 as thermally activated with a diode activation energy E_a and exponential prefactor J_{00}, following

$$J_0(T) = J_{00}\exp\left(\frac{-E_a}{n(T)k_BT}\right). \quad \text{(Equation 2)}$$

As detailed in the following, E_a and J_{00} constitute important indicators of the device behavior and limitations; hence, their extraction via Arrhenius plots representing Equation 2 is essential. Note S1 and Figure S1 provide further details in that regard along with the theory related to Equation 1 and the extraction procedure for the different parameters, as well as a discussion regarding the negligible impact of R_s and R_{sh}. The following section treats the temperature evolution of the diode parameters and the implications regarding material properties and dominant recombination paths.

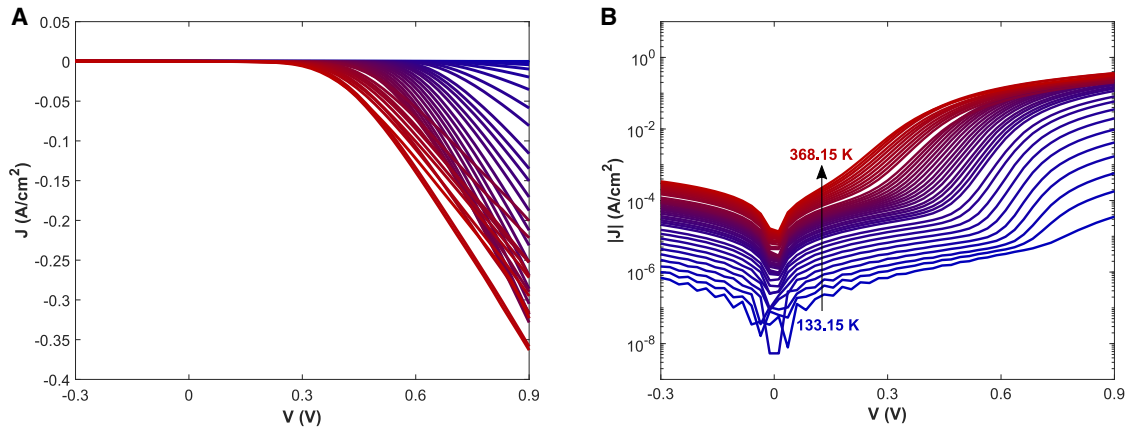

Figure 1. Dark temperature-dependent current-voltage (JVT) dataset

Dark current-voltage curves of the A1 sample at different temperatures in either (A) linear scale or (B) logarithmic scale in absolute value for the current. The color gradient ranges from blue at the lowest temperature of 133.15 K to red at the highest temperature of 368.15 K, as emphasized by the black arrow, with 10 K steps from 133.15 to 233.15 K and 5 K steps from 233.15 to 368.15 K.

Dark JVT in forward bias to study recombination mechanisms

The dark JVT curves are shown in Figure 1, corresponding to $J_{ph}(V,T) = 0$ in Equation 1, in which all parameters are extracted following the procedure detailed in Note S1 and Figure S1. At 300 K, $J_0 = 6.66 * 10^{-8} A/cm^2$, $n = 1.56$, $R_s = 0.89\ \Omega.cm^2$, and $R_{sh} = 3{,}340\ \Omega.cm^2$, as reported previously for an equivalent baseline with excellent performance.[2]

Applicability of the single diode model

Equation 2 provides that the single diode model applies if an Arrhenius plot of $\ln(J_0)$ vs. $1/k_BT$ is linear on a temperature range in which $n(T)$ is constant (Figures 2A and 2B), meaning that E_a can be extracted as the linear slope for an arbitrary J_{00}. However, in real devices, the condition for n to be unchanged with temperature is rarely met,[14,18–21] as shown in Figure 2B for the sample studied here. To overcome this issue, a modified Arrhenius plot of $n(T) * \ln(J_0)$ vs. $1/k_BT$ is drawn in Figure 2C to account for the variations of n with temperature when extracting E_a and J_{00} as in the following:

$$n(T) * \ln(J_0(T)) = n(T) * \ln(J_{00}) + \frac{-E_a}{k_B T}, \qquad \text{(Equation 3)}$$

which is equivalent to Equation 2. From this representation, estimates of $E_a = 1.15\ eV$ and $J_{00} = 1.85 * 10^5 A/cm^2$ are obtained by linear regression. In this work, the temperature-dependent ideality factor, noted as either n or $n(T)$ and shown in Figure 2B, is distinguished from the true ideality factor n',[22] defined as the average of n above 223.15 K, where it is constant. In the present case, $n' = 1.56$, which allows one to compute J_0 predictions: $J_{0,pred} = J_{00} * \exp\left(\frac{-E_a}{n' k_B T}\right)$. As shown in Figure S2, those predictions have a relative error below 1% in the whole temperature range from 368.15 K down to 223.15 K, hence called the model applicability (MA) region and represented as red symbols or lines in all relevant figures. This temperature range encompasses room temperature, so that the model outcomes concern the behavior of the studied sample in real operation conditions, i.e., at 300 K. The temperature independence of E_a due to the benign character of band gap and potential fluctuations for the devices under study is demonstrated in Note S2, which has two implications. First, all temperature variations in Equation 3 are accounted for by the modified Arrhenius plot in Figure 2C, which is therefore sufficient to estimate $E_a = 1.15\ eV$ and $J_{00} = 1.85 * 10^5 A/cm^2$ accurately in the MA region. Second, compared to previous findings,[14] the studied kesterite absorbers are likely to possess more homogeneous composition, phase, lattice strain, and/or donor/acceptor compensation degree across their surface but also narrower band tails and lower-density point defects,[14,23,24] all considered favorable regarding device performance.

The dark JVT response of sample A1 in Figure 2 is also observed in additional samples A2, A3, and B, with similar model agreement, as shown in Figures S3 and S4, which extends the validity of the methodology developed herein. The resulting estimates of n', J_0 at 300 K, E_a, and J_{00} for A2, A3, and B are comparable to those obtained for A1, as summarized in Table S1. This hints at a common behavior of kesterite solar cells processed with that baseline (samples A1, A2, and A3) and its variations (sample B). The analysis is pursued below for the specific case of sample A1.

Below 233.15 K, $\ln(J_0)$ is no longer linear with $1/k_BT$, while $n(T)$ increases significantly (Figures 2A and 2B), meaning that the single diode model, even using the modified Arrhenius plot, is no longer applicable. This is obvious from the divergence of the J_0 predictions in that temperature range in Figure S2. For this reason, it is denoted herein as an out-of-model (OoM) region, represented as blue symbols or lines in all relevant figures. The divergence with the single diode model in the OoM region means other mechanisms come into play and additions should be made to take them into account. This is discussed at the end of this section, after the thorough analysis of the MA range to unveil the implications of E_a, $n(T)$, and J_{00} regarding material properties and device limitations.

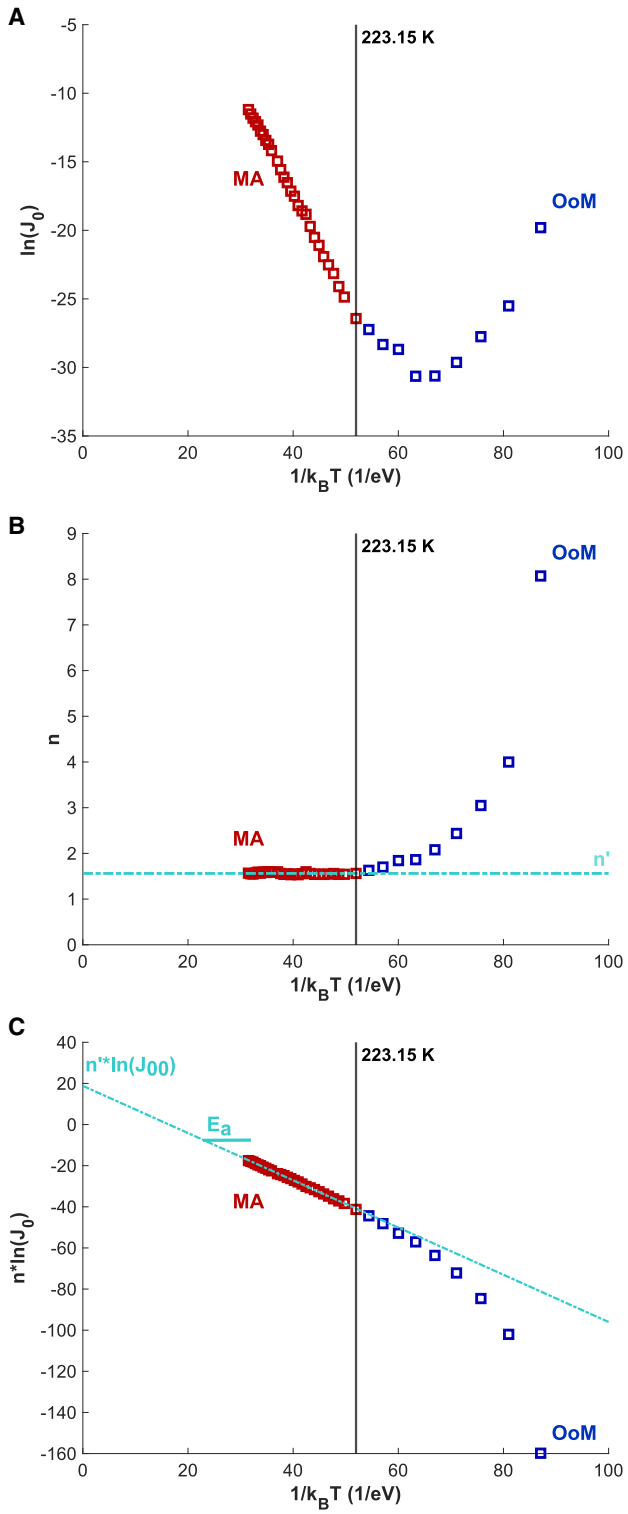

Figure 2. Temperature dependence of dark diode parameters

Evolution of (A) the saturation current density J_0, (B) the ideality factor n, and (C) their product $n * \ln(J_0)$ in the function of the inverse thermal energy $1/k_BT$ for the A1 sample. Data points are shown as red and blue squares for respectively the model applicability (MA) and out-of-model (OoM) ranges described in the text. The temperature of 223.15 K delimiting these ranges is represented by a solid black vertical line. The value of the true ideality factor $n' = 1.56$ and the linear fit to $n * \ln(J_0)$ leading to $E_a = 1.15\,eV$ and $J_{00} = 1.85 * 10^5 A/cm^2$ are shown as cyan dashed lines.

Activation energy E_a

First, the value of E_a is essential as it theoretically encloses information about the main V_{oc}-limiting factor, which is key to enhance performance, especially in the case of kesterites. The typical analysis consists in comparing the value of E_a to the absorber band gap E_g, and the usual conclusion if $E_a < E_g$ is observed is that IF recombination is dominating the diode response. In practice, grain boundary recombination or a cliff-like HJ band alignment can also lead to $E_a < E_g$.[14,22] In this case, $E_a \simeq E_g = 1.15\,eV$, which relates to a positive conduction band offset at the HJ[22] or the so-called spike-like band alignment, usually considered a condition for efficient chalcogenide/CdS solar cells. Another consequence is that the presence of Fermi level pinning can be ruled out, since E_a is much greater than the HJ hole barrier at 0 V $\phi_b^{p,0}$. Indeed, $E_a = 1.15\,eV \gg \phi_b^{p,0} = qV_{bi}(1-\theta) + (E_F - E_V) \simeq qV_{bi} + \frac{E_g}{2} - k_BT\ln\left(\frac{N_A}{n_i}\right) = 0.6\,eV$, in which the HJ built-in voltage $V_{bi} = 0.4\,V$ and the absorber carrier concentration $N_A = 10^{15} cm^{-3}$ are estimated from capacitance-voltage (CV) measurements,[2] in agreement with the theoretical value of $(E_F - E_V) = 0.2\,eV$ from another study.[10] The theta parameter $\theta = \frac{\epsilon_{abs} N_A}{\epsilon_{abs} N_A + \epsilon_{buff} N_D}$ quantifies the asymmetric/abrupt character of the HJ, with the dielectric permittivity of the absorber $\epsilon_{abs} = 9\epsilon_0$[10] (resp. the buffer $\epsilon_{buff} = 10\epsilon_0$[25]) and doping density N_D of the buffer. Even in the extreme case $\theta = 0$ leading to the highest possible value for $\phi_b^{p,0}$ and meaning $N_D \gg N_A$, $\phi_b^{p,0}$ remains largely smaller than E_a. This confirms the absence of Fermi level pinning for the studied device and suggests another culprit for its improvable V_{oc} of 497 mV in Table S3, as discussed in the following. However, since the carrier concentration of CdS layers grown on kesterite layers is difficult to accurately determine and not reported in the literature, the quantity N_D is left as undetermined at this point and θ is considered as a parameter.

Ideality factor n

Observing $n(T) = n' = 1.56 > 1$ in MA provides another insight into the dominant recombination type as well as certain material properties. Indeed, theory provides that $n > 1$ could be caused either by tail-like energy-distributed defects in the bulk of the absorber[20,21] or by IF-limited recombination.[22] In the former case, the model states that n should depend on temperature, which is not observed herein, and does not cover the possibility of Gaussian-distributed defects usually probed by admittance spectroscopy.[26,27] In the latter case, n is correctly predicted as temperature invariant, but its constant value in MA is such that $n' = \frac{1}{1-\theta} = 1.56$, leading to $\theta = 0.36$ and $N_{D,th} = 1.6 * 10^{15} cm^{-3}$, which appears relatively lower than usual expectations in the case of a CdS buffer, hinting that a more realistic model might be required. To cope with the limitations of both theoretical models and provide a more refined prediction of the ideality factor value in the function of defect properties and buffer doping, SCAPS-1D[17] simulations are performed.

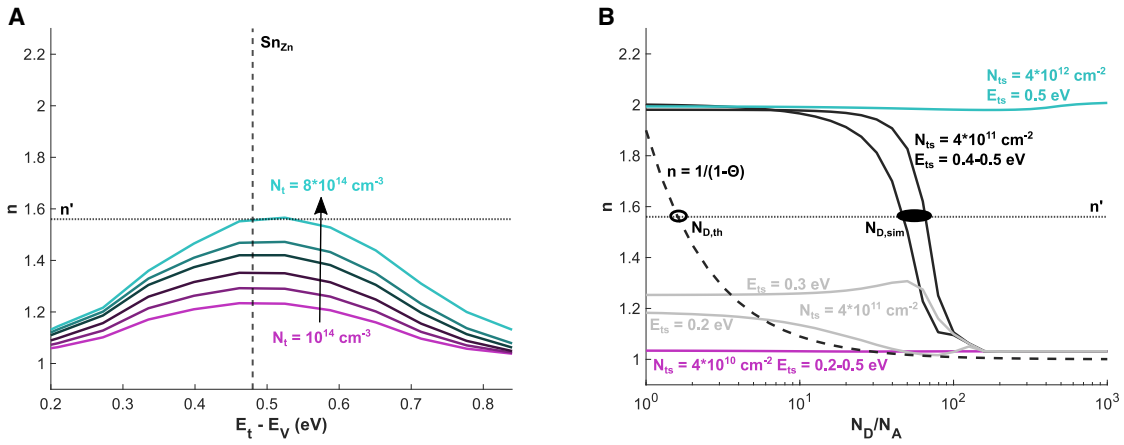

Figure 3. SCAPS-1D modeling of the ideality factor *n*

(A) Results of the SCAPS-1D simulations for a bulk defect in the absorber with Gaussian energy distribution width of 100 meV and for varying central energy level E_t and density N_t (case 1 in the text). The six different curves correspond to N_t values progressively ranging from $1 * 10^{14} cm^{-3}$ (pink solid line) to $8 * 10^{14} cm^{-3}$ (cyan solid line) with intermediate values of 1.7, 2.8, 4.6, and 6 in units of $10^{14} cm^{-3}$. The vertical dashed line represents the calculated energy level of the Sn_{Zn} antisite defect.[10] The horizontal dashed line represents $n' = 1.56$.

(B) Results of the SCAPS-1D simulations for a single defect at the heterojunction interface for varying depth E_{ts} and density N_{ts} (case 2 in the text). The black solid lines illustrate deep defects at a fixed median density of $N_{ts} = 4 * 10^{11} cm^{-2}$, the gray solid lines represent shallow defects at a fixed median density of $N_{ts} = 4 * 10^{11} cm^{-2}$, while the cyan and pink solid lines respectively depict higher and lower N_{ts}. The filled black ellipse highlights the range $N_{D,sim} = 4.7 - 6.6 * 10^{16} cm^{-3}$ of N_D values predicted by SCAPS-1D simulations to match $n' = 1.56$. The black dashed curve depicts the theoretical interface model $n = \frac{1}{1-\theta}$ detailed in the text, which intercepts the experimental n value at a buffer doping of $N_{D,th} = 1.6 * 10^{15} cm^{-3}$ as shown by the hollow black circle. The horizontal dashed line represents $n' = 1.56$.

The main objective is to determine whether a qualitative, or at best semi-quantitative, agreement can be reached in two different defect configurations used throughout this section, either a Gaussian bulk defect with energy distribution width E_{char}, volume defect density N_t, and energy level E_t in the kesterite absorber (case 1) or a single IF defect with surface defect density N_{ts} and energy level E_{ts} at the kesterite/CdS HJ (case 2). In the latter configuration, the buffer doping N_D is also an important parameter. The model parameters for the SCAPS-1D simulations are provided in Table S2, as inspired by a previous study,[28] while further details and results are given in Note S3 and Figure S5.

In case 1, i.e., when recombination is taking place via bulk defects, the most important parameters are N_t and E_t, with their impact on n illustrated in Figure 3A, while E_{char} and N_D exhibit negligible influence as mentioned in Note S3 and illustrated in Figures S5A and S5B. One can observe that n is logically closer to 1 as the defect is shallower and hence less active with regard to recombination, while it is maximum for E_t close to the midgap. Moreover, the $E_t - n$ curves are scaled up as N_t progressively approaches N_A. At this point, the simulations thus provide qualitative information about the properties of a defect that would explain n' close to 1.5. Indeed, Figure 3A demonstrates that such a true ideality factor value could be explained by a Gaussian defect in the bulk of the absorber with a density comparable to the absorber doping, an energy level close to the midgap and $\sigma_n = 10^{-13} cm^2$. Such characteristics are precisely close to those of the Sn_{Zn} antisite donor defect identified to be highly detrimental to performance from density functional theory (DFT) calculations,[10] with its (2+/+) state located at $E_t = 480\,meV$ above the valence band edge (shown in Figure 3A) and an electron capture cross section close to the one used here. Sn_{Zn} could thus be a relevant candidate as a dominant recombination center inducing $n' = 1.56$, further supported by its critical role in kesterite devices similar to the studied sample[3] and the reports of equivalent defect depths around 500 meV from deep-level transient spectroscopy.[26,27]

In case 2, i.e., when recombination is taking place via IF defects, the ratio between the doping on the p side N_A and the n side N_D is important since both layers can now exchange carriers. In other terms, $N_D/N_A \propto \frac{1-\theta}{\theta}$ determines the inversion strength at the HJ surface. Considering $N_A = 10^{15} cm^{-3}$, the evolution of n in the function of N_D/N_A in Figure 3B is obtained for various combinations of N_{ts} and E_{ts}. Further details about the parameter configurations not matching n' (cyan, gray, and pink lines in Figures 3B and S5C) are provided in Note S3. In contrast, the intermediate density $N_{ts} = 4 * 10^{11} cm^{-2}$ configurations provide closer agreement with n', especially for deep levels between 400 and 500 meV (black lines in Figure 3B), thereby defining a range $N_{D,sim} = [47; 66] N_A = [4.7 * 10^{16}; 6.6 * 10^{16}]\, cm^{-3}$ of corresponding N_D values. In these curves, the strengthening of the n-type inversion at the HJ surface for higher buffer carrier concentration explains their characteristic transition from a higher n value, scaling down with the defect depth, for $N_D \ll 10^{17} cm^{-3}$ to a constant plateau with $n \simeq 1$ for $N_D \gg 10^{17} cm^{-3}$. Thus, according to simulations, relatively deep traps at the HJ IF may be responsible for $n' = 1.56$, provided that the CdS doping is higher than the theoretically predicted $N_{D,th} = 1.6 * 10^{15} cm^{-3}$ from $n = \frac{1}{1-\theta}$[22] as shown in

Figure 3B. Experimentally determining the energy depth and density of defects located at the HJ IF is tedious; hence, the values predicted by simulations herein cannot be directly compared to literature reports.

To cope with this issue, a third simulation structure is developed to simulate the impact of a defect located close to the HJ surface, thus depending on the n-type inversion while having the properties of a bulk defect in the kesterite absorber that can be compared to either experimental or computational results. To do so, a thin defective layer (DL) is added at the ACZTSSe/CdS IF, constituting a hybrid situation between case 1 and case 2. The volume defect density in the DL is obtained by dividing the initial IF defect density of $N_{ts} = 4 * 10^{11} cm^{-2}$ by the DL thickness t_{DL}, leading to $N_{DL} = N_{ts}/t_{DL}$. The defect depth is $E_{ts} = 500\,meV$ so that it is close to the Sn_{Zn} antisite level,[10] while the DL thickness is $t_{DL} = 10\,nm$, providing $N_{DL} = 4 * 10^{17} cm^{-3}$. Even though N_{DL} is higher than the absorber doping, its concentration along a much thinner layer does not impede proper functioning of the simulation model as in the bulk situation (case 1). From the comparison shown in Figure S5D, it appears that n behaves similarly in the function of the HJ doping ratio in both cases, with the only difference being that the CdS doping required to transition from the high-n high-recombination case to the low-n low-recombination case is roughly four times higher for the DL. For the present case, this demonstrates that, if there exists a thin layer in the kesterite absorber close to the HJ surface with high defect densities, n may be greater than 1 even at very high CdS doping above $10^{17} cm^{-3}$. Since it is not possible with the sole analysis of E_a and n' to determine if the dominant recombination path is bulk, IF, or DL related, the dark analysis is pursued with the study of J_{00} in MA.

Saturation current exponential prefactor J_{00}

Indeed, J_{00} can be studied independently of n and E_a to possibly confirm the hypotheses drawn herein. In general, J_{00} depends on the localization of the dominant recombination path along the absorber thickness: quasi-neutral zone, space-charge region (SCR), or HJ IF. The first and second both happen in the absorber bulk. Still, it is well established that the maximum recombination point in thin-film devices is located in the SCR, where the electron and hole densities are equal; hence, it contributes much more to the whole recombination than carriers diffusing through the quasi-neutral zone, especially within low-mobility low-lifetime materials such as kesterites.[29,30]

Therefore, in the bulk (case 1), only SCR recombination is considered in this work, for which J_{00} at 300 K can be expressed as the following[14,18]:

$$J_{00,SCR}(300K) = \pi k_B 300 \sqrt{\frac{\epsilon_{abs} N_{C,abs} N_{V,abs}}{2 q V_{bi} N_A}} \frac{1}{\tau_n}. \quad \text{(Equation 4)}$$

Following the numerical development in Note S4, $J_{00} = 1.85 * 10^5 A/cm^2$ provides $\tau_n = 0.12\,ns$. Even though standard time-resolved photoluminescence (TRPL) decays in kesterites are rather of the order of 1–10 ns,[2,30,31] careful analysis of such experiments reveals that such a sub-nanosecond estimate may better correspond to the actual minority lifetime in the ACZTSSe absorber.[29] In the aforementioned case of Sn_{Zn} with $\sigma_n = 9.3 * 10^{-14} cm^2$,[10] $\tau_n = 0.12\,ns$ would require a bulk defect density of $9 * 10^{15} cm^{-3}$. From the SCAPS-1D simulations, a purely bulk defect extending across the whole absorber thickness with $N_t = 9 * 10^{15} cm^{-3} > N_A$ would not be compatible with decent efficiency or $n' = 1.56$, while surpassing the experimentally estimated densities from defect spectroscopy techniques.[26] Still, such N_t values could be reconciled with the observed ideality factor if the corresponding defects rather extend along a thin DL close to the HJ, according to the developed SCAPS-1D model. To verify this assumption, the theoretical model for IF-limited J_{00} can be used to check for consistency, since the SCAPS-1D structures for defects either in a DL or at the HJ IF prove to behave similarly.

For IF recombination (case 2) at the HJ with spike-like alignment and no Fermi level pinning, J_{00} is theoretically predicted independent of temperature and determined by the hole surface recombination velocity S_p in cm/s at that surface[22]:

$$J_{00,IF} = q S_p N_A \left(\frac{N_{C,buff} N_{V,abs}}{N_D N_A} \right)^{1-\theta}. \quad \text{(Equation 5)}$$

The quantitative matching between Equation 5 and $J_{00} = 1.85 * 10^5 A/cm^2$ provides two S_p values, i.e., $S_{p,sim} = 5.0 - 6.4 * 10^2 cm/s$ and $S_{p,th} = 9 * 10^3 cm/s$, respectively for the two estimations $N_{D,sim} = 4.7 - 6.6 * 10^{16}$ and $N_{D,th} = 1.6 * 10^{15} cm^{-3}$ obtained in the previous section, as detailed in Note S4 and Figure S6. Their difference by one order of magnitude emphasizes the importance of determining the doping of the CdS buffer grown on kesterite absorbers for further studies. Assuming $\sigma_p = 10^{-15} cm^2$,[11] the estimated $S_{p,sim}$ values correspond to N_{ts} on the order of $10^{11} cm^{-2}$. This aligns rather well with the defect density ranges used in the SCAPS-1D analysis of n above in either the IF or the DL case, thus supporting their possible role as the dominant recombination channel in the studied device. As a final step of this dark JVT analysis, the OoM range is investigated to possibly unveil further insight into the device behavior.

Tunneling-enhanced recombination at low temperature

As mentioned above, for temperatures below 223.15 K, the single diode model is no longer applicable as such. This is attested by the non-linearity of $\ln(J_0)$ in the Arrhenius plot as well as the increase of n in the OoM region in Figures 2A and 2B. In that temperature range, the parameters E_a and J_0 extracted from the MA can no longer predict the evolution of J_0 with $1/k_B T$, as observed in Figure S2. Still, some preliminary conclusions of the MA range analysis can help to build an analysis framework for the OoM region. Indeed, it is demonstrated above that high-density defects located at the HJ IF and possibly extended as a thin DL could explain the E_a, n, and J_{00} values in MA and hence that the IF-limited recombination formalism should be applied to understand the device under study. Considering this, a unified model for the bulk tunneling-enhanced recombination (bulk-TER) and IF-tail mechanisms allows one to explain the increase of n at lower temperatures and the divergence from the model, as detailed in Note S5 and illustrated in Figures S7 and S8. The primary contribution to $n(T)$ in the OoM range resides in bulk-TER, for which high defect densities on the order of $10^{18} cm^{-3}$ must be considered to fit the experimental data. This is well aligned with

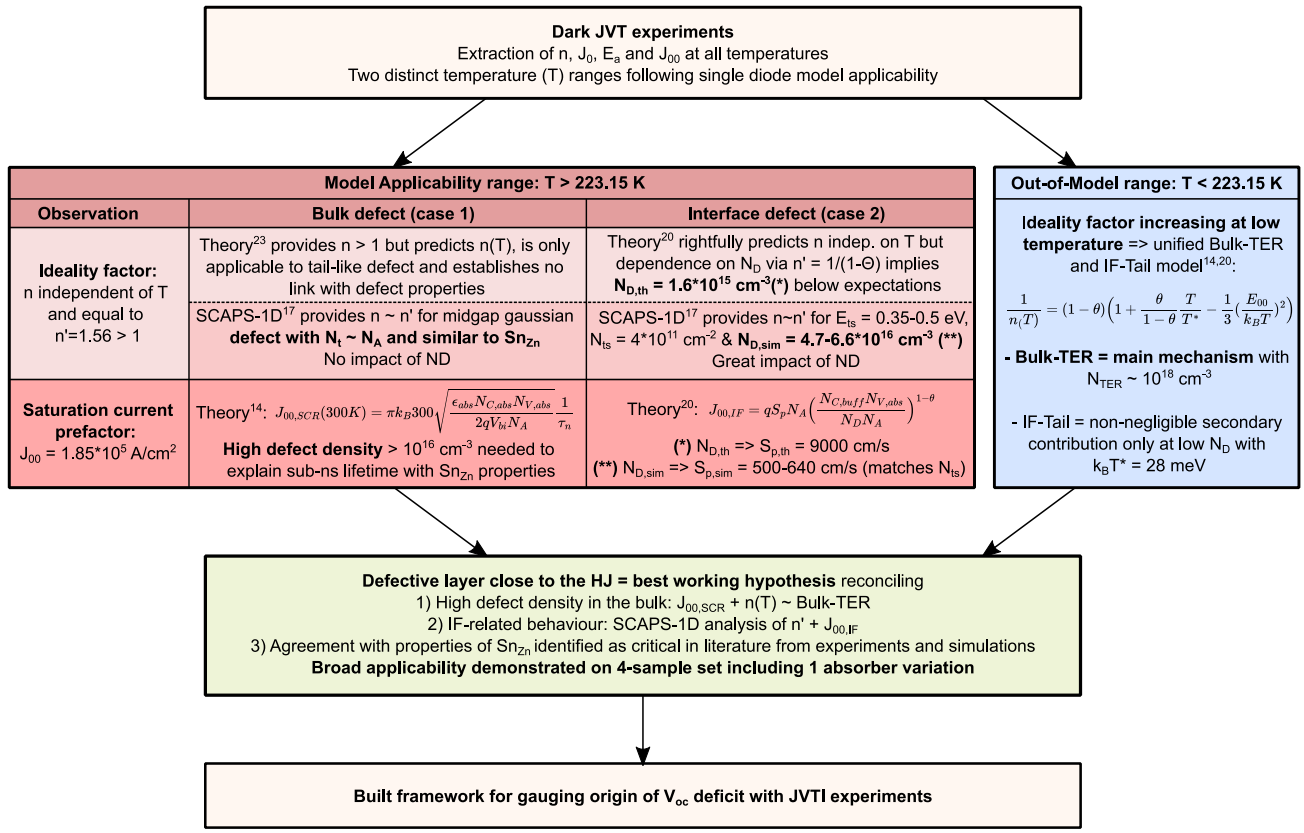

Figure 4. Summary of the dark JVT analysis

Schematic overview of the main models used in the reasoning to develop the dark JVT analysis and the most important resulting conclusions. Reference numbers provided in superscript are referring to the main text reference list.

the DL defect concentration level extrapolated from the SCAPS-1D IF model. One necessary condition for the TER mechanism to dominate is the presence of a strong electric field, which is precisely the case in the SCR close to the HJ, further confirming the key role of this region with regard to recombination mechanisms for the studied sample.

DL as the best working hypothesis

The close agreement of the measured device behavior with the single diode model is demonstrated in a broad temperature range including 300 K, at which $J_0 = 6.66 * 10^{-8} A/cm^2$ and $n' = 1.56$. The extracted diode temperature dependency parameters $E_a = 1.15\,eV$ and $J_{00} = 1.85 * 10^5 A/cm^2$ combined with the true ideality factor $n' = 1.56$ lead to highly accurate predictions of $J_0(T)$ with relative error below 1%, indicating that their analysis should allow one to draw meaningful hypotheses about the dominant recombination channel in the device under study. Observing $E_a = E_g$ confirms the desired spike-like conduction band alignment at the HJ while ruling out the possibility of Fermi-level pinning, but does not allow one to discriminate between bulk- and IF-limited recombination. Still, based on the combined analysis of n and J_{00}, this study proposes a hybrid model in which a thin defect-rich kesterite layer at the IF with the CdS buffer is the main recombination path. This hypothesis allows one to reconcile (1) the high bulk defect densities on the order of $10^{17} - 10^{18} cm^{-3}$ implied by both the $J_{00,SCR}$ model and the predicted increase of n at low temperatures under the bulk-TER formalism, (2) the IF-related behavior highlighted by both the SCAPS-1D-driven qualitative analysis justifying $n > 1$ even at high CdS doping and the quantitative matching with $J_{00,IF}$, and (3) the semi-quantitative agreement with the Sn_{Zn} defect, as described from first-principle simulations,[10] which is experimentally designated as most detrimental in state-of-the-art kesterite devices.[3] These observations and hypotheses arguably also apply to comparative samples A2, A3, and B, since their dark JVT response is highly similar to that of the A1 device on which the above development is built. The corresponding reasoning as well as the underlying models are summarized in Figure 4. The location of this DL very close to the HJ IF stresses the importance of the buffer carrier concentration in determining the diode quality and aligns with the ideality factor improvement under illumination discussed in the next section. This kesterite layer concentrating high defect densities arguably dominates non-radiative recombination in the studied samples, but its chemical origin is still unresolved at this point. Previous studies have suggested the existence in CIGS absorbers of a superficial layer rich in Cu vacancies (V_{Cu}), called an ordered vacancy compound (OVC), typically

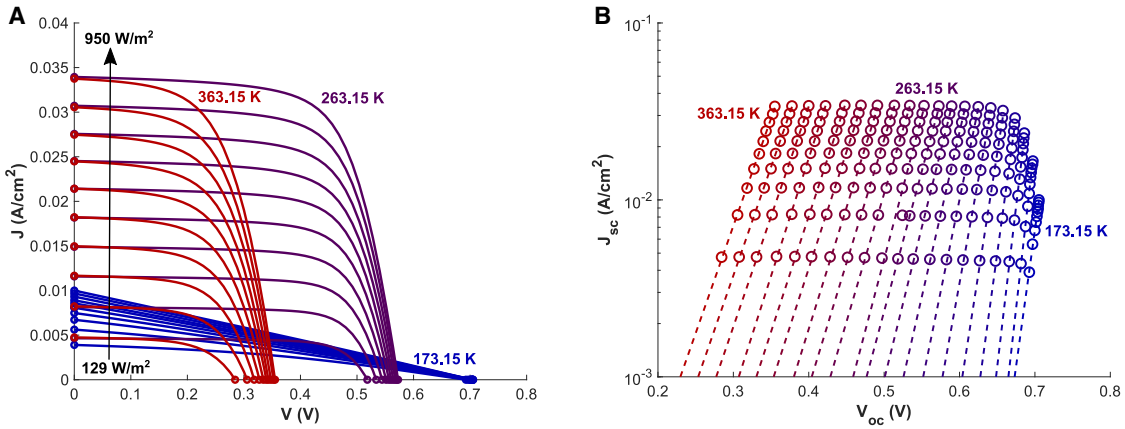

Figure 5. Temperature- and light-intensity-dependent current-voltage dataset

(A) Current-voltage curves in linear scale from 129 to 950 W/m^2 illumination intensity (black arrow) for the A1 sample at three example temperatures (363.15 K in red, 263.15 K in purple, and 173.15 K in blue), with J_{sc} and V_{oc} values indicated by circles along the axes.

(B) $\ln(J_{sc}) - V_{oc}$ characteristics at all measurement temperatures for the A1 sample depicted as circles in a color gradient from blue at the lowest temperature of 173.15 K to red at the highest temperature of 363.15 K, with their respective linear fitting shown as a dashed line of the same color. The temperature step between lines is 10 K.

a few tens of nanometers thick and playing an important role regarding the device functioning.[32,33] The same hypothesis could potentially apply to kesterite materials, historically inspired by CIGS and also including V_{Cu} defects potentially clustered with Sn_{Zn}, among others.[10,11]

Light-intensity-dependent JVT to gauge performance limitations

With the dark analysis completed and a hypothesis drawn about the main recombination path, it is interesting to verify if the A1 device behavior under light can similarly be predicted to assess the relationship with performance limitations. To do so, the JVTI dataset obtained under various light intensities and the corresponding V_{oc} and short-circuit current density (J_{sc}) values are used (Figure 5A). The corresponding measurement procedure is detailed in the methods.

J_{sc}-V_{oc} methodology

In this section, the J_{sc}-V_{oc} methodology[34] is applied to the JVTI measurements in order to extract the same parameters as for the dark JVT analysis. In particular, at each temperature, a $\ln(J_{sc}) - V_{oc}$ characteristic is obtained by varying the illumination intensity from 129 (0.13 sun) to 950 W/m^2 (0.95 sun), the linear fitting of which provides J_{0L} and n_L as respectively the intercept and the inverse slope (Figure 5B). The "L" subscript is used to distinguish the JVTI estimates from the dark JVT estimates. At 300 K, $J_{0L} = 6.15 * 10^{-9} A/cm^2$ and $n_L = 1.2$, which are both lower than in the dark, attesting an improvement of the diode optoelectronic quality under illumination. Then, the temperature dependence of both of them is analyzed to estimate the parameters E_{aL} and J_{00L}. The impact of R_s on V_{oc} is null, since there is no voltage drop across it for zero current at open circuit, while R_{sh} does not modify the value of J_{sc} for zero voltage at short circuit. Both would respectively influence J_{sc} and V_{oc} only for extreme values, which is ruled out in the previous section.

Diode parameters under light

Similar to the dark JVT experiments, there is a temperature range above 263.15 K in which $\ln(J_{0L})$ vs. $1/k_BT$ is linear and $n_L = n'_L = 1.20$ is constant, as shown in Figures 6A and 6B. In this range, also called MA, the J_{0L} predictions have a relative error below 1% as illustrated in Figures S9A and S9B, indicating an as-good agreement with the single diode model as in the dark. Divergence with the single diode model is also observed under light at low temperature, i.e., in the OoM range below 263.15 K, in a way that is not predicted by the models used herein. This is out of the scope of this section, which aims at evaluating the performance impairments in MA and shall thus require further investigations. The modified Arrhenius plot is herein used again (Figure 6C) to extract $E_{aL} = 1.17\,eV$ and $J_{00L} = 7.77 * 10^7 A/cm^2$. Observing $E_{aL} = 1.17\,eV \simeq E_a = 1.15\,eV = E_g$ confirms the weak dark-light discrepancy and suggests that the illuminated HJ diode has the same characteristics as in the dark, i.e., a spike-like conduction band alignment without Fermi level pinning. As also similarly concluded in the dark JVT analysis, Figure S9C demonstrates that all temperature variations are accounted for by $n_L(T)$ so that α_L is nearly equal to 0 and E_{aL} and J_{00L} can be considered mostly temperature independent. The similarity in the device behavior in MA in both dark and light conditions is further emphasized when directly comparing the evolution of the respective diode parameters in Figure 6. This feature is usually not observed among inorganic thin-film solar cells still in development, such as kesterites.[14,35] This very point attests the closer-to-ideal behavior of the device under study as well as the more mature state of recent molecular ink kesterite baselines.[12] Still, $n'_L < n'$ is observed in Figure 6, suggesting changes in the junction properties upon illumination. A possible culprit is the CdS buffer doping N_D, which has been reported to change under light in chalcogenide devices under the "CdS photodoping effect."[36–43] In the IF or DL formalism developed above using both theoretical and SCAPS-1D models, an increase in the carrier concentration of

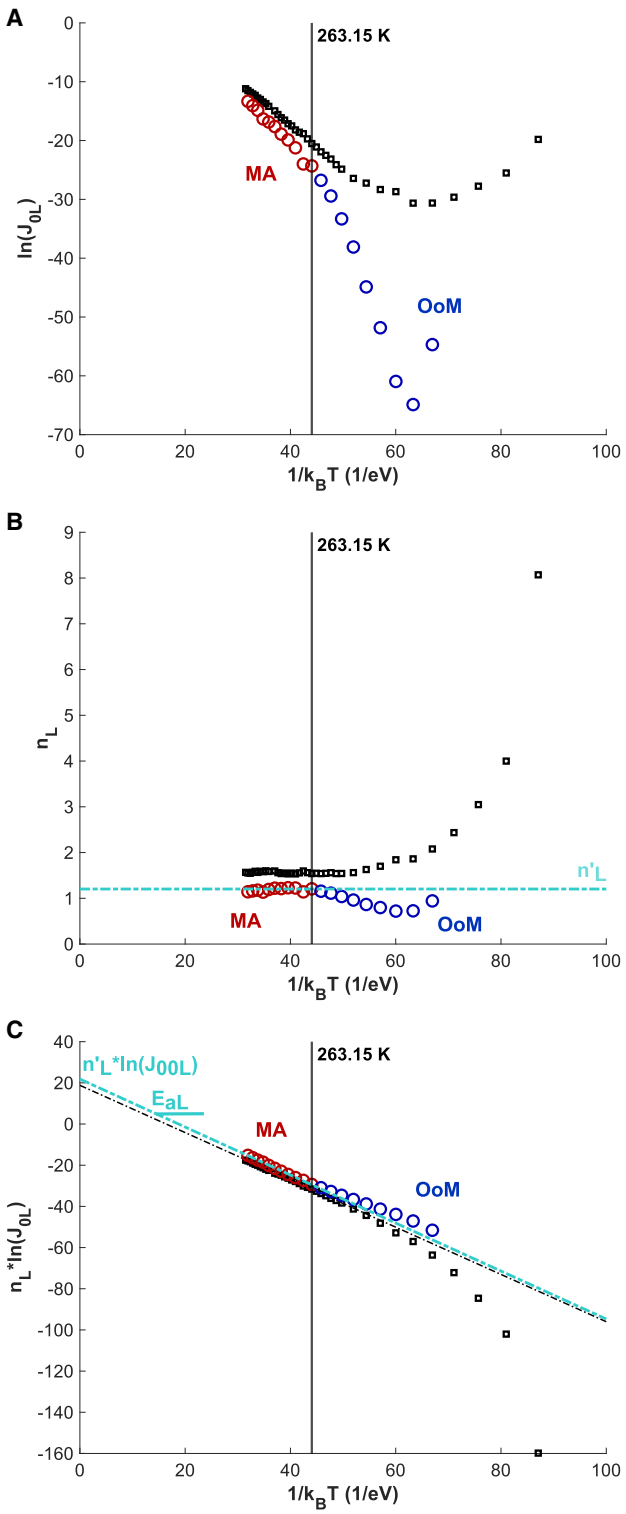

Figure 6. Temperature dependence of light diode parameters

Evolution of (A) the saturation current density J_{0L}, (B) the ideality factor n_L, and (C) their product $n_L * \ln(J_{0L})$ in the function of the inverse thermal energy $1/k_BT$ for the A1 sample, all obtained via the J_{sc}-V_{oc} methodology. Data points are shown as red and blue circles for respectively the model applicability (MA) and the out-of-model (OoM) ranges described in the text. The temperature of 263.15 K delimiting these ranges is represented by a solid black vertical line. The value of the true ideality factor $n'_L = 1.2$ and the linear fit to $n_L * \ln(J_{0L})$ leading to $E_{aL} = 1.17\,eV$ and $J_{00L} = 7.77 * 10^7 A/cm^2$ are shown as cyan dashed lines. The dark results already shown in Figure 2 are shown again as black squares and black dashed lines to facilitate comparison.

the buffer layer would indeed provide a decrease in the true ideality factor n'_L. This is illustrated in Figure S10 for either the theoretical IF model[22] or the IF and DL SCAPS-1D models implemented in this work, all predicting that even minute N_D changes may be responsible for large n improvements. In other terms, the DL hypothesis drawn from the dark analysis would also justify the reduction of n under light through the photodoping-induced increase in the CdS carrier concentration.

After developing the hypothesis of the thin defect-rich kesterite layer at the HJ surface, it is important to gauge its impact on the device performance in real operation conditions, i.e., at room temperature and close to 1 sun irradiance. The main indicator of the significance of such a non-radiative recombination-related feature is logically V_{oc}, widely recognized as the primary culprit of the kesterite solar cells' limited efficiency. The linear extrapolation of V_{oc} at all light intensities in MA until 0 K provides activation energies $qV_{oc,0K}$ contained between 1.14 and 1.16 eV in Figure 7A, thus corresponding very well to the absorber band gap E_g. The observed $qV_{oc,0K} \simeq E_g$ and weak V_{oc} rollover are important updates of the recent kesterite solar cells' behavior[2,13] in comparison with previous studies.[14,34,44] The nearly perfect match between $qV_{oc,0K}$, E_{aL}, and E_a as well as the rollover starting at the temperature of 263.15 K delimiting the MA and OoM ranges implies that V_{oc} is governed by the same mechanism as the light diode parameters, proposed to be a DL in this work. Thus, in order to estimate the corresponding losses in V_{oc} and the respective contributions of each parameter, V_{oc} is expressed in the function of temperature and at a given light intensity as

$$V_{oc,pred}(T) = E_{aL} - \frac{n'_L k_B T}{q} \ln\left(\frac{J_{00L}}{\eta_C(V_{oc},T) J_{sc}(T)}\right). \quad \text{(Equation 6)}$$

This expression originates in imposing open-circuit conditions and neglecting parasitic resistances in Equation 1, implying zero total current at a voltage equal to V_{oc}, while developing J_{0L} through Equation 2 using the diode parameters extracted under light. It also considers a voltage-dependent collection efficiency $J_{ph}(V_{oc}, T) = \eta_C(V_{oc}, T) J_{sc}(T)$.[14,35] As thoroughly detailed in Note S6 and depicted in Figure S11, using the extracted parameters at 300 K ($E_{aL} = 1.17\,eV$, $n'_L = 1.2$, $J_{00L} = 7.77 * 10^7 A/cm^2$, and $\eta_C(V_{oc}) = 46\%$), the V_{oc} predictions in Equation 6 are obtained with high qualitative and quantitative agreement as compared to the experimental data. This allows high-confidence estimation of the individual contributions to the V_{oc} deficit through a comparison with an ideal case in which $E_{aL} = E_g$, $n'_L = 1$, $J_{00L} = J_{00,ideal}$, and $\eta_C(V_{oc}) = 100\%$. The corresponding V_{oc}-deficit individual contributions are represented in Figure 7B in comparison with the corresponding V_{oc} value at 0.95 sun and associated Shockley-Queisser (SQ) limit and further discussed in Note S6. A major gain of 363 mV in V_{oc} resides in the diode parameters n'_L and J_{00L} related to

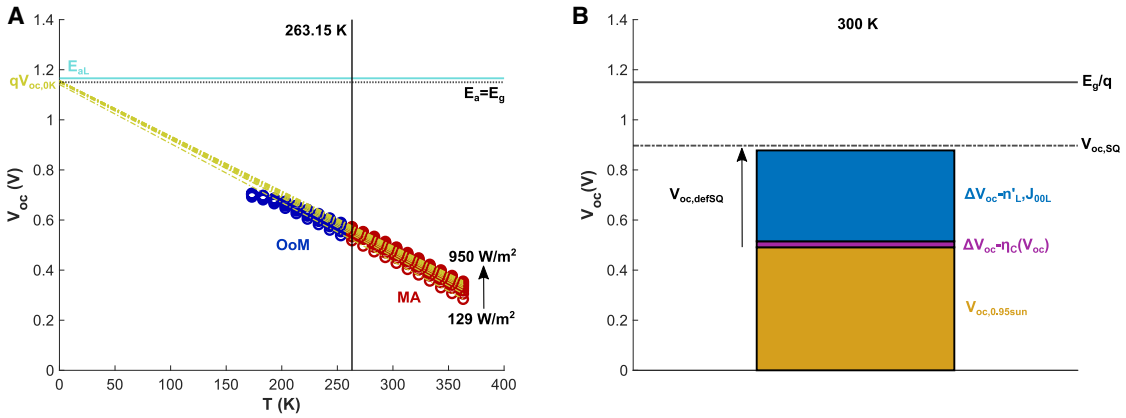

Figure 7. Temperature evolution and potential gains in V_{oc}

(A) Evolution of V_{oc} in the function of the temperature T for sample A1 at different light intensities indicated by the black arrow, with data shown as red and blue circles for respectively the model applicability (MA) and out-of-model (OoM) ranges as described in the text. The horizontal solid cyan (resp. dashed black) line represents the light diode activation energy E_{aL} = 1.17 *eV* (resp. dark diode activation energy equal to the absorber band gap $E_a = E_g$ = 1.15 *eV*) at 300 K. The dashed yellow lines depict the linear fits to the V_{oc} data in MA, leading to an extrapolated value at 0 K $qV_{oc,0K}$ between 1.14 and 1.16 eV. The temperature of 263.15 K delimiting the MA and OoM ranges is represented by a solid black vertical line.

(B) Graphical representation of the experimental V_{oc} at 0.95 sun (orange bar) compared to the potential gains due to voltage-dependent collection efficiency $\Delta V_{oc-\eta_C(V_{oc})}$ (purple bar) and improvement of the light ideality factor and saturation current density prefactor $\Delta V_{oc-n'_L J_{00L}}$ (blue bar), for the A1 sample. The black dashed and solid lines respectively represent the SQ limit $V_{oc,SQ}$ and the corresponding band gap E_g/q. The black arrow highlights the V_{oc} deficit according to the SQ limit $V_{oc,defSQ}$.

defect-assisted recombination, while $\eta_C(V_{oc})$, usually associated with series resistance and low mobility-lifetime product,[14,35] entails only a secondary contribution of 24 *mV*. The analysis conducted herein further highlights J_0 as the main culprit for the significant V_{oc} deficit in recent kesterite baselines for which radiative losses have been largely mitigated.[12] Similar to the dark JVT analysis, the JVTI formalism developed herein also applies to sample A2 and leads to highly similar parameter estimates, as shown in Figure S12 and Table S1. Therefore, in the studied devices, V_{oc} losses are largely dominated by non-radiative recombination, hypothesized to mainly take place in a thin DL at the HJ IF and quantified by the ideality factor *n* and saturation current density prefactor J_{00}, while the imperfect collection efficiency plays only a secondary role. Given the applicability of the presented analysis in both dark and light across multiple devices with different absorbers, the resulting conclusions may potentially affect a broad range of kesterite devices. The adoption of specific defect passivation strategies in the ACZTSSe/CdS HJ vicinity should thus be investigated in the future so as to mitigate the associated V_{oc} deficit.

Dark JVT in reverse bias to explore origin of shunt

Besides the V_{oc} losses, the fill factor (FF) deficit of kesterite solar cells is the second most important performance limitation. It is impacted not only by the diode parameters studied above but also by the device JV response in low forward and reverse bias, where currents happen to be linearly dependent on voltage yet exponentially dependent on temperature, as illustrated by the temperature evolution of R_{sh} in Figure 8A. Such a log-linear dependence of R_{sh} with temperature cannot be solely explained through ohmic conduction or other common transport mechanisms, as discussed in Note S7. Instead, trapping-detrapping (TD) appears as a more likely candidate, resolving both voltage and temperature dependencies while being already reported for kesterite materials.[29] It consists in a thermally activated variation of the material conductivity related to trapping of free carriers within shallow band-gap states. In the case of kesterite solar cells, it is reported to happen via shallow traps close to the conduction band and may be one of the keys to reconcile the widely observed discrepancy between measured TRPL decay and actual minority carrier lifetime.[29] For these reasons, R_{sh} is herein considered as governed by TD in the dark. Following the mathematical development in Note S7, an Arrhenius plot of $\ln(R_{sh}T^2)$ vs. $1/k_BT$ should yield the energy level E_{TD} of the defect through which TD is occurring as its linear slope. This is illustrated in Figure 8B. As illustrated in Figure 8B, the existence of three distinct slopes at high, medium, and low temperatures is observed, with corresponding E_{TD} values of respectively E_{aTD1} = 130 *meV*, E_{aTD2} = 103 *meV* and E_{aTD3} = 60 *meV*, the latter in agreement with previously reported estimates.[29] The transition between the different activation energies as temperature varies indicates a change in the defect through which TD is taking place. In particular, the fact that E_{TD} successively decreases with temperature could relate to the simultaneous downward movement of the Fermi level as well as the decrease in the thermal energy k_BT required by electrons in the conduction band to be captured and emitted by the shallow neighboring states. Under the current formalism, the shallow trap seemingly dominating dark shunt currents via TD at room temperature is 103 *meV* away from the conduction band. Such a close-to-band edge trap depth could correspond to DFT-computed Zn_{Cu} donors with low formation energy,[11] the shallower (+/0) state of Sn_{Zn},[10] band tailing-related $Sn_{Zn}+2Cu_{Zn}$ complexes and out-of-plane $(Cu_{Zn}+Zn_{Cu})_{\perp}$ clusters,[9] or experimentally

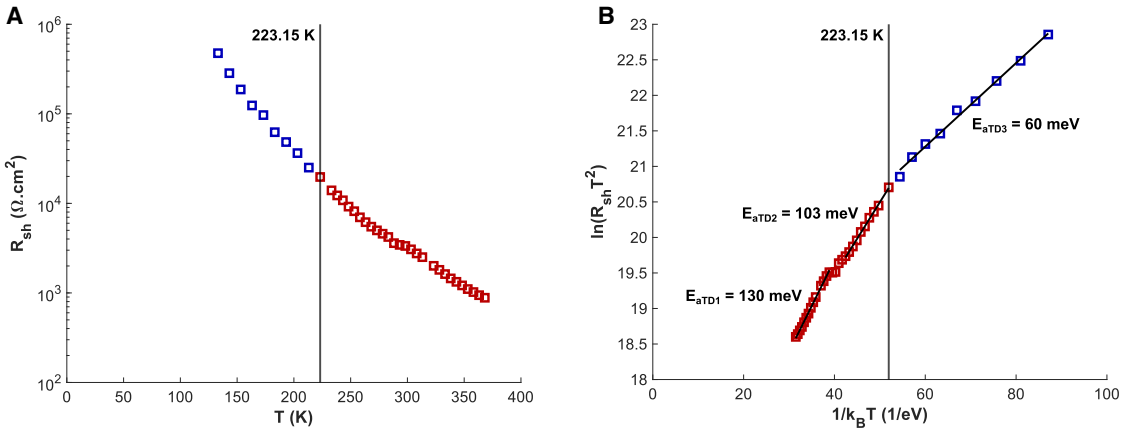

Figure 8. Temperature-dependent shunt resistance

Evolution of (A) R_{sh} in the function of the temperature T and of (B) $\ln(R_{sh}T^2)$ in the function of the inverse thermal energy $1/k_BT$ following the dark extraction for the A1 sample, with data shown as red and blue squares for respectively the model applicability (MA) and the out-of-model (OoM) ranges. The black solid lines represent the linear fittings in the three ranges described in the text, providing the three activation energies related to trapping-detrapping (TD). The temperature of 223.15 K delimiting the MA and OoM ranges is represented by a solid black vertical line.

characterized shallow defect levels.[45–47] The TD process appears responsible for the exponential temperature dependence of the linearly voltage-dependent reverse currents and dominates the value of R_{sh} in the dark, not only for the A1 sample but also for all other studied devices around room temperature, as shown in Figure S13. Even though the study of this mechanism upon illumination would require further experiments, the contributions of TD to reverse currents are likely also affecting the response of such devices under light and thus eventually impacting the FF. Therefore, a careful inspection of the related processes is needed in the future to pursue further performance improvements and device physics understanding.

DISCUSSION

A thorough analysis of dark- and light-intensity-dependent current-voltage measurements at different temperatures emphasizes the need for an update of the device modeling for recent kesterite baselines based on molecular ink chemical routes. Their higher optoelectronic quality characterized by benign band tailing and potential fluctuations allows excellent agreement with the standard single diode model, facilitating the understanding and prediction of their closer-to-ideal behavior in both dark and light conditions. Through a combination of well-established semi-analytical models and simulations, the values and temperature dependencies of all parameters were studied, pointing toward a thin DL at the absorber/buffer IF as the main recombination channel at room temperature. Qualitative and semi-quantitative agreement was obtained with the Sn_{Zn} donor properties recently highlighted as one of the most detrimental intrinsic point defects in the kesterite lattice. The key role played by the CdS carrier concentration with regard to recombination at the HJ IF was defined more precisely by SCAPS-1D simulations. Divergences with the single diode model at low temperatures can be explained by tunneling-enhanced recombination. The remarkable weakness of dark-light discrepancy for the studied thin-film solar cell allows one to gauge the various contributions to the still-too-significant V_{oc} deficit. The critical importance of the hypothesized DL is emphasized as it largely determines the value of the ideality factor n and the saturation current density prefactor J_{00}, both responsible for the resulting large V_{oc} improvements still to be accomplished. To do so, passivation schemes at the HJ IF and strategies to increase the carrier concentration in the buffer seem promising. Besides, the impact of HJ annealing and of alternative buffer materials with different doping levels regarding the MA and the formation of the DL should be further assessed. Specific studies aiming at verifying the existence of such a DL and determining its chemical nature need to be pursued in the future through depth-dependent analysis of composition and optoelectrical response. It appears especially important as the validity of the whole analysis and the resulting conclusions extends across multiple devices, including different kesterite absorber compositions. This is also true for the reverse bias analysis, for which this work eventually suggests that carrier TD via shallow states may dominate reverse currents in the investigated samples. This phenomenon likely contributes to shunt leakages, which are particularly essential with regard to performance of indoor PV systems.

METHODS

Sample processing and characteristics

The kesterite absorber in the studied devices was prepared following a molecular ink baseline recipe targeting around 15% Ag and less than 10% S, corresponding to $E_g = 1.15\,eV$ and $E_u \simeq 20\,meV$, with high reproducibility and good device performance.[2,13] On top of the absorber were successively deposited a 50 nm CdS buffer by chemical bath, 40 nm i-ZnO and 150 nm indium tin oxide (ITO) window layers by RF sputtering, and 500 nm Ag grid by thermal evaporation, for a total device area of 0.23 cm^2 determined by hand scribing over the Ag

grid mask, without antireflection coating. Samples A1, A2, and A3 were repetitions of this whole process and hence highly comparable as attested by their similar PV figures of merit in Table S3. These values were all extracted at 25°C under an AM1.5G spectrum with 950 W/m^2 (0.95 sun) illumination intensity, explained by the 5% glass window loss subtracted from the 1,000 W/m^2 solar simulator output as described in the JVTI measurement conditions below. Sample B differs from the other devices by its kesterite absorber being 10% Li alloyed, which induces marginally higher band gap[2] while exhibiting slightly reduced performance as shown in Table S3. Sample B is thus useful to highlight the validity of the presented methodology to devices with different absorbers. All samples had power conversion efficiencies ranging roughly between 10% and 12%, which made their comparison relevant and aligned with state-of-the-art solution-processed Ag-alloyed kesterite solar cell baselines.[2,3,6,7,13]

Measurement procedure

The JVTI setup relies on a Keithley 6430 source meter used in a four-point configuration to realize current-voltage measurements. It is connected via coaxial cables to a temperature-controlled heating and cooling stage from Microptik (MHCS600-P), enclosed in a vacuum-sealed box equipped with an N_2 circuit for cooling down. The box is placed directly below an LED-based G2V AAA solar simulator, with the incident light reaching the whole device area of 0.23 cm^2 through a glass window cast within the box top cover. The incident irradiance on the outside of the measurement box is AM1.5G 1,000 W/m^2, the magnitude of which is uniformly scaled up or down to tune the illumination intensity. The measurement procedure is as follows:

(1) A verification measurement is performed with the box sealed in both dark and light to ensure the quality of contacts and the proper working of the device. The loss of incident power through the box glass window at the sample position is evaluated to be 5% at any light intensity. Taking this into account provides the close-to-1 sun irradiance reference of 950 W/m^2 (0.95 sun) used throughout this work and especially in the JVTI analysis.

(2) The actual measurement starts by cooling down the sample to the lowest temperature. Once reached, and for each subsequent temperature point, a waiting time of at least 3 min is applied before any action. Dark and light intensity-dependent measurements are done separately to exclude the possible influence of light soaking on the dark measurements.
   - For dark JVT experiments, the temperature is increased in steps of 10 K from 133.15 K (−130°C) to 233.15 K (−40°C) and in steps of 5 K from 233.15 K (−40°C) to the highest temperature of 368.15 K (95°C), corresponding to 37 different temperatures.
   - For JVTI experiments, where measurement time is more critical, the temperature is increased in steps of 10 K from 173.15 K (−90°C) to the highest temperature of 363.15 K (90°C), corresponding to 20 different temperatures.

(3) At each temperature point stabilized after the waiting time, JV curves are measured from −0.3 to 0.9 V in 5 s with a 0.05 s dwell time, either in the dark or at 10 different light intensities from 129 W/m^2 (0.13 sun) to 950 W/m^2 (0.95 sun).

RESOURCE AVAILABILITY

Lead contact

Requests for further information and resources should be directed to and will be fulfilled by the lead contact, Romain Scaffidi (romain.scaffidi@imec.be).

Materials availability

This study did not generate new materials.

Data and code availability

- All other data reported in this paper will be shared by the lead contact upon request.
- Any additional information required to reanalyze the data reported in this paper is available from the lead contact upon request.

ACKNOWLEDGMENTS

This research received funding from the European Union's H2020 Framework Programme for Research and Innovation under grant agreement number 952982 (CUSTOM-ART) and 866018 (SENSATE: low-dimensional semiconductors for optically tunable solar harvesters) as well as from the Renew-PV European COST action (CA21148). R.S. thanks the Research Foundation Flanders (FWO) for funding through the Fundamental Research PhD Fellowship (1178024N) and a travel grant for a long stay abroad (V462623N). Y.G. thanks the European Union's H2020 Framework Programme for Research and Innovation under the Marie Skłodowska-Curie grant agreement number 10115148. A. J.-A. and E.S. acknowledge funding from the Agencia Estatal de Investigación, MICINN Spain, project ACT-FAST (PCI2023-145971-2) from the CETP-Partnership Program 2022. A.B. is thankful for the grant SIR/2022/001011 from SERB India. Z.J.L.-K. acknowledges the Spanish Ministry of Science and Innovation for the Ramon y Cajal Fellowship (RYC2021-033239-I). E.S. acknowledges financial support from the Spanish Ministry of Science and Innovation from the CURIO-CITY project (PID2023-148976OB-C41). This work was part of the Maria de Maetzu Units of Excellence Programme CEX2023-001300-M, funded by MCIN/AEI/10.13039/501100011033. E.S. acknowledges the ICREA Academia program.

AUTHOR CONTRIBUTIONS

R.S. performed conceptualization, methodology, validation, formal analysis, investigation, data curation, software, writing – original draft, writing – review & editing, and visualization. A.J.-A. performed conceptualization, validation, investigation, resources, and writing – review & editing. Y.G. performed conceptualization, investigation, resources, and writing – review & editing. G.B. performed conceptualization, validation, supervision, project administration, writing – review & editing, and funding acquisition. A.B. performed conceptualization, methodology, investigation, and writing – review & editing. Z.J.L.-K. performed conceptualization and writing – review & editing. E.S. performed resources, supervision, project administration, and funding acquisition. D.F. performed conceptualization, validation, supervision, and writing – review & editing. B.V. performed supervision, project administration, and funding acquisition.

DECLARATION OF INTERESTS

The authors declare no competing interests.

SUPPLEMENTAL INFORMATION

Supplemental information can be found online at https://doi.org/10.1016/j.newton.2025.100198.

Received: March 5, 2025
Revised: April 23, 2025
Accepted: July 11, 2025
Published: August 7, 2025

REFERENCES

1. Green, M.A., Dunlop, E.D., Yoshita, M., Kopidakis, N., Bothe, K., Siefer, G., Hao, X., and Jiang, J.Y. (2025). Solar Cell Efficiency Tables (Version 65). Progress in Photovoltaics. *33*, 3–15. https://doi.org/10.1002/pip.3867.
2. Gong, Y., Jimenez-Arguijo, A., Medaille, A.G., Moser, S., Basak, A., Scaffidi, R., Carron, R., Flandre, D., Vermang, B., Giraldo, S., et al. (2024). Li-Doping and Ag-Alloying Interplay Shows the Pathway for Kesterite Solar Cells with Efficiency Over 14%. Adv. Funct. Mater. *34*, 2404669. https://doi.org/10.1002/adfm.202404669.
3. Shi, J., Wang, J., Meng, F., Zhou, J., Xu, X., Yin, K., Lou, L., Jiao, M., Zhang, B., Wu, H., et al. (2024). Multinary alloying for facilitated cation exchange and suppressed defect formation in kesterite solar cells with above 14% certified efficiency. Nat. Energy *9*, 1095–1104. https://doi.org/10.1038/s41560-024-01551-5.
4. Li, J., Huang, J., Ma, F., Sun, H., Cong, J., Privat, K., Webster, R.F., Cheong, S., Yao, Y., Chin, R.L., et al. (2022). Unveiling microscopic carrier loss mechanisms in 12% efficient Cu2ZnSnSe4 solar cells. Nat. Energy *7*, 754–764. https://doi.org/10.1038/s41560-022-01078-7. https://www.nature.com/articles/s41560-022-01078-7.
5. Gong, Y., Zhang, Y., Zhu, Q., Zhou, Y., Qiu, R., Niu, C., Yan, W., Huang, W., and Xin, H. (2021). Identifying the origin of the V_{oc} deficit of kesterite solar cells from the two grain growth mechanisms induced by Sn 2+and Sn 4+precursors in DMSO solution. Energy Environ. Sci. *14*, 2369–2380. https://doi.org/10.1039/D0EE03702H.
6. Zhou, J., Xu, X., Wu, H., Wang, J., Lou, L., Yin, K., Gong, Y., Shi, J., Luo, Y., Li, D., et al. (2023). Control of the phase evolution of kesterite by tuning of the selenium partial pressure for solar cells with 13.8% certified efficiency. Nat. Energy *8*, 526–535. https://doi.org/10.1038/s41560-023-01251-6. https://www.nature.com/articles/s41560-023-01251-6.
7. Gong, Y., Zhu, Q., Li, B., Wang, S., Duan, B., Lou, L., Xiang, C., Jedlicka, E., Giridharagopal, R., Zhou, Y., et al. (2022). Elemental de-mixing-induced epitaxial kesterite/CdS interface enabling 13%-efficiency kesterite solar cells. Nat. Energy *7*, 966–977. https://doi.org/10.1038/s41560-022-01132-4.
8. Wang, A., He, M., Green, M.A., Sun, K., and Hao, X. (2023). A Critical Review on the Progress of Kesterite Solar Cells: Current Strategies and Insights. Adv. Energy Mater. *13*, 2203046. https://doi.org/10.1002/aenm.202203046.
9. Crovetto, A., Kim, S., Fischer, M., Stenger, N., Walsh, A., Chorkendorff, I., and Vesborg, P.C.K. (2020). Assessing the defect tolerance of kesterite-inspired solar absorbers. Energy Environ. Sci. *13*, 3489–3503. https://doi.org/10.1039/D0EE02177F.
10. Kim, S., Márquez, J.A., Unold, T., and Walsh, A. (2020). Upper limit to the photovoltaic efficiency of imperfect crystals from first principles. Energy Environ. Sci. *13*, 1481–1491. https://doi.org/10.1039/D0EE00291G.
11. Chen, W., Dahliah, D., Rignanese, G.M., and Hautier, G. (2021). Origin of the low conversion efficiency in Cu2ZnSnS4 kesterite solar cells: the actual role of cation disorder. Energy Environ. Sci. *14*, 3567–3578. https://doi.org/10.1039/D1EE00260K.
12. Wong, L., Hadke, S., Su, Z., Meng, Q., Xin, H., Wu, S., Liang, G.X., and Shao, Z. (2024). Approaching the Theoretical Efficiency of Kesterite Solar Cells: Analysis of Radiative and Non-Radiative Losses in Cu2ZnSn(S,Se)4. Preprint at Research Square. https://www.researchsquare.com/article/rs-5136540/v1.
13. Scaffidi, R., Gong, Y., Jimenez-Arguijo, A., Medaille, A.G., Suresh, S., Brammertz, G., Giraldo, S., Puigdollers, J., Flandre, D., Vermang, B., and Saucedo, E. (2024). Tuning the bandgap without compromising efficiency: Ambient solution processing of Ge-alloyed (Ag,Cu)2Zn(Sn,Ge)(S,Se)4 kesterite thin-film solar cells. Mater. Today Energy *46*, 101715. https://doi.org/10.1016/j.mtener.2024.101715.
14. Hages, C.J., Carter, N.J., Agrawal, R., and Unold, T. (2014). Generalized current-voltage analysis and efficiency limitations in non-ideal solar cells: Case of Cu2ZnSn(SxSe1-x)4 and Cu2Zn(SnyGe1-y)(SxSe1-x)4. J. Appl. Phys. *115*, 234504. https://doi.org/10.1063/1.4882119.
15. Scaffidi, R., Birant, G., Brammertz, G., De Wild, J., Flandre, D., and Vermang, B. (2023). Ge-alloyed kesterite thin-film solar cells: previous investigations and current status – a comprehensive review. J. Mater. Chem. A *11*, 13174–13194. https://doi.org/10.1039/D3TA01218B.
16. Gong, Y., Jimenez-Arguijo, A., Caño, I., Scaffidi, R., Malerba, C., Valentini, M., Payno, D., Navarro-Güell, A., Segura-Blanch, O., Flandre, D., et al. (2025). Attaining 15.1% Efficiency in Cu_2 $ZnSnS_4$ Solar Cells Under Indoor Conditions Through Sodium and Lithium Codoping. Sol. RRL *9*, 2400756. https://doi.org/10.1002/solr.202400756.
17. Burgelman, M., Nollet, P., and Degrave, S. (2000). Modelling polycrystalline semiconductor solar cells. Thin Solid Films *361–362*, 527–532. https://doi.org/10.1016/S0040-6090(99)00825-1.
18. Rau, U., and Schock, H.W. (1999). Electronic properties of Cu(In,Ga)Se 2 heterojunction solar cells-recent achievements, current understanding, and future challenges. Appl. Phys. Mater. Sci. Process *69*, 131–147. https://doi.org/10.1007/s003390050984.
19. Rau, U., Jasenek, A., Schock, H.W., Engelhardt, F., and Meyer, T. (2000). Electronic loss mechanisms in chalcopyrite based heterojunction solar cells. Thin Solid Films *361–362*, 298–302. https://doi.org/10.1016/S0040-6090(99)00762-2.
20. Walter, T., Herberholz, R., and Schock, H.W. (1996). Distribution of Defects in Polycrytalline Chalcopyrite Thin Films. SSP *51*, 309–316. https://doi.org/10.4028/www.scientific.net/SSP.51-52.309.
21. Walter, T., Menner, R., Köble, C., and Schock, H.W. (1994). Characterization and junction performance of highly efficient ZnO/CdS/$CuInS_2$ thin film solar cells (Proc. 12th EC Photovoltaic Solar Energy Conference), pp. 1755–1758.
22. Scheer, R. (2009). Activation energy of heterojunction diode currents in the limit of interface recombination. J. Appl. Phys. *105*, 104505. https://doi.org/10.1063/1.3126523.
23. Werner, J.H., Mattheis, J., and Rau, U. (2005). Efficiency limitations of polycrystalline thin film solar cells: case of Cu(In,Ga)Se2. Thin Solid Films *480–481*, 399–409. https://doi.org/10.1016/j.tsf.2004.11.052.
24. Rau, U., and Werner, J.H. (2004). Radiative efficiency limits of solar cells with lateral band-gap fluctuations. Appl. Phys. Lett. *84*, 3735–3737. https://doi.org/10.1063/1.1737071.
25. Böer, K.W. (2013). Handbook of the Physics of Thin-Film Solar Cells (Springer Berlin Heidelberg). https://doi.org/10.1007/978-3-642-36748-9.
26. Li, J.V., Kuciauskas, D., Young, M.R., and Repins, I.L. (2013). Effects of sodium incorporation in Co-evaporated Cu2ZnSnSe4 thin-film solar cells. Appl. Phys. Lett. *102*, 163905. https://doi.org/10.1063/1.4802972.
27. Kheraj, V., Lund, E.A., Caruso, A.E., Al-Ajmi, K., Pruzan, D., Miskin, C., Agrawal, R., Beall, C., Repins, I., and Scarpulla, M.A. (2016). Minority carrier electron traps in CZTSSe solar cells characterized by DLTS and DLOS. In 2016 IEEE 43rd Photovoltaic Specialists Conference (PVSC) (IEEE), pp. 2195–2199. https://doi.org/10.1109/PVSC.2016.7750024.
28. Jimenez-Arguijo, A., Medaille, A.G., Navarro-Güell, A., Jimenez-Guerra, M., Tiwari, K.J., Placidi, M., Mkehlane, M.S., Iwuoha, E., Perez-Rodriguez, A., Saucedo, E., et al. (2023). Setting the baseline for the modelling of Kesterite solar cells: The case study of tandem application. Sol. Energy Mater. Sol. Cell. *251*, 112109. https://doi.org/10.1016/j.solmat.2022.112109.
29. Hages, C.J., Redinger, A., Levcenko, S., Hempel, H., Koeper, M.J., Agrawal, R., Greiner, D., Kaufmann, C.A., and Unold, T. (2017). Identifying the Real Minority Carrier Lifetime in Nonideal Semiconductors: A Case Study of Kesterite Materials. Adv. Energy Mater. *7*, 1700167. https://doi.org/10.1002/aenm.201700167.

30. Grossberg, M., Krustok, J., Hages, C.J., Bishop, D.M., Gunawan, O., Scheer, R., Lyam, S.M., Hempel, H., Levcenco, S., and Unold, T. (2019). The electrical and optical properties of kesterites. JPhys Energy *1*, 044002. https://doi.org/10.1088/2515-7655/ab29a0.

31. Gokmen, T., Gunawan, O., Todorov, T.K., and Mitzi, D.B. (2013). Band tailing and efficiency limitation in kesterite solar cells. Appl. Phys. Lett. *103*, 103506. https://doi.org/10.1063/1.4820250.

32. Wei, S.H., and Zhang, S.B. (2005). Defect properties of CuInSe2 and CuGaSe2. J. Phys. Chem. Solid. *66*, 1994–1999. https://doi.org/10.1016/j.jpcs.2005.10.003.

33. Zhao, Y., Yuan, S., Chang, Q., Zhou, Z., Kou, D., Zhou, W., Qi, Y., and Wu, S. (2021). Controllable Formation of Ordered Vacancy Compound for High Efficiency Solution Processed Cu(In,Ga)Se_2 Solar Cells. Adv. Funct. Mater. *31*, 2007928. https://doi.org/10.1002/adfm.202007928.

34. Gunawan, O., Gokmen, T., and Mitzi, D.B. (2014). Suns- *VOC* characteristics of high performance kesterite solar cells. J. Appl. Phys. *116*, 084504. https://doi.org/10.1063/1.4893315.

35. Hegedus, S., Desai, D., and Thompson, C. (2007). Voltage dependent photocurrent collection in CdTe/CdS solar cells. Progress in Photovoltaics. *15*, 587–602. https://doi.org/10.1002/pip.767.

36. Igalson, M., Bodegård, M., and Stolt, L. (2003). Reversible changes of the fill factor in the ZnO/CdS/Cu(In,Ga)Se2 solar cells. Sol. Energy Mater. Sol. Cell. *80*, 195–207. https://doi.org/10.1016/j.solmat.2003.06.006.

37. Chien, F.S.S., Herawati, A., He, M.Y., Huang, C.Y., and Chen, C.Y. (2020). Optical Responses of the Heterojunctions in Cu_2 ZnSn(S,Se)$_4$ Solar Cells Studied by Electric Modulus Spectroscopy. ACS Appl. Electron. Mater. *2*, 796–801. https://doi.org/10.1021/acsaelm.9b00852.

38. Pudov, A.O., Kanevce, A., Al-Thani, H.A., Sites, J.R., and Hasoon, F.S. (2005). Secondary barriers in CdS–CuIn1-xGaxSe2 solar cells. J. Appl. Phys. *97*, 064901. https://doi.org/10.1063/1.1850604.

39. Xin, H., Katahara, J.K., Braly, I.L., and Hillhouse, H.W. (2014). 8% Efficient Cu_2 ZnSn(S,Se)$_4$ Solar Cells from Redox Equilibrated Simple Precursors in DMSO. Adv. Energy Mater. *4*, 1301823. https://doi.org/10.1002/aenm.201301823.

40. Li, J., Wang, H., Luo, M., Tang, J., Chen, C., Liu, W., Liu, F., Sun, Y., Han, J., and Zhang, Y. (2016). 10% Efficiency Cu2ZnSn(S,Se)4 thin film solar cells fabricated by magnetron sputtering with enlarged depletion region width. Sol. Energy Mater. Sol. Cell. *149*, 242–249. https://doi.org/10.1016/j.solmat.2016.02.002.

41. Mitzi, D.B., Gunawan, O., Todorov, T.K., Wang, K., and Guha, S. (2011). The path towards a high-performance solution-processed kesterite solar cell. Sol. Energy Mater. Sol. Cell. *95*, 1421–1436. https://doi.org/10.1016/j.solmat.2010.11.028.

42. Hsu, W.C., Repins, I., Beall, C., DeHart, C., Teeter, G., To, B., Yang, Y., and Noufi, R. (2013). The effect of Zn excess on kesterite solar cells. Sol. Energy Mater. Sol. Cell. *113*, 160–164. https://doi.org/10.1016/j.solmat.2013.02.015.

43. Liu, F., Yan, C., Sun, K., Zhou, F., Hao, X., and Green, M.A. (2017). Light-Bias-Dependent External Quantum Efficiency of Kesterite Cu_2 ZnSnS_4 Solar Cells. ACS Photonics *4*, 1684–1690. https://doi.org/10.1021/acsphotonics.7b00151.

44. Moore, J., Hages, C.J., Carter, N., Agrawal, R., and Lundstrom, M. (2013). The physics of Vbi-related IV crossover in thin film solar cells: Applications to ink deposited CZTSSe. In 2013 IEEE 39th Photovoltaic Specialists Conference (PVSC) (IEEE), pp. 3255–3259. https://doi.org/10.1109/PVSC.2013.6745146.

45. Gunawan, O., Gokmen, T., Warren, C.W., Cohen, J.D., Todorov, T.K., Barkhouse, D.A.R., Bag, S., Tang, J., Shin, B., and Mitzi, D.B. (2012). Electronic properties of the Cu2ZnSn(Se,S)4 absorber layer in solar cells as revealed by admittance spectroscopy and related methods. Appl. Phys. Lett. *100*, 253905. https://doi.org/10.1063/1.4729751.

46. Khadka, D.B., Kim, S., and Kim, J. (2015). A Nonvacuum Approach for Fabrication of Cu_2 ZnSnSe_4/In_2 S_3 Thin Film Solar Cell and Optoelectronic Characterization. J. Phys. Chem. C *119*, 12226–12235. https://doi.org/10.1021/acs.jpcc.5b03193.

47. Koeper, M.J., Hages, C.J., Li, J.V., Levi, D., and Agrawal, R. (2017). Metastable defect response in CZTSSe from admittance spectroscopy. Appl. Phys. Lett. *111*, 142105. https://doi.org/10.1063/1.4996283.